Microsystem Technologies (2023) 29:809–821
https://doi.org/10.1007/s00542-023-05459-0

TECHNICAL PAPER

Design and analysis of a novel low RF MEMS switch with low pull-in voltage and high capacitance ratio

Zhongliang Deng[1] · Chengqi Lai[1] · Jiali Zhou[2] · Yucheng Wang[1]

Received: 18 August 2022 / Accepted: 19 April 2023 / Published online: 28 April 2023
© The Author(s), under exclusive licence to Springer-Verlag GmbH Germany, part of Springer Nature 2023

Abstract
This paper designs and analyzes a novel RF MEMS capacitive switch with a high on/off capacitance ratio and low pull-in voltage. Compared with general capacitive RF MEMS switches, the switch adopts a new type of spring support structure, which reduces the spring coefficient of elasticity and forms a low pull-in voltage. By adding an H-shaped floating metal layer above the switch dielectric layer, the on/off capacitance ratio is improved without affecting the predetermined structure of the switch and without thin dielectrics or high dielectric constant materials. Finally, the pull-in voltage of the switch is 4.4 V, and the switching time is 22 µs. When the switch operates at 27 GHz, the isolation of the switch is – 50 dB, the insertion loss is − 0.2 dB, and the switch capacitance ratio is 89. The designed switch shows good working performance.

1 Introduction

With the development of wireless communication technology and the continuous improvement of communication standards in the past few decades, millimeter-wave communication and reconfigurable technology have become the focus of wireless communication. It has also made the RF-MEMS switch a research hotspot in recent years because of its potential application scenarios (Zareie et al. 2013). In the high-frequency range, compared to PIN diodes and FETs (field-effect transistors), RF MEMS switches have the advantages of good linearity, high isolation, low insertion loss, and frequency bandwidth (Mousavi et al. 2021). However, problems such as high pull-in voltage and low on/off capacitance ratio still restrict the development of RF MEMS switches (Dalal et al. 2021). High pull-in voltages can cause compatibility issues between RF MEMS switches and associated control circuits, while low on/off capacitance ratios can degrade the device's RF performance.

In the past literature, switches with good performance have been reported. Al-Dahleh et al. (2010) and Fouladi et al. (2010) improved the switch on/off capacitance ratio using a warped switch beam. However, this method cannot guarantee the consistency of the switch during processing. Angira et al. (2013) and Persano et al. (2010) use high dielectric constant materials to achieve high capacitance ratios. To reduce the pull-in voltage, Xu et al. (2018) realized a switch with a pull-in voltage of 14 V installed on a reconfigurable frequency antenna. Gopalan and Kommuri (2018) developed a triangular-shaped RF MEMS switch for the fabrication of micro-phase shifters with a pull-in voltage of 5.6 V. Angira and Rangraet (2015) use a floating metal RF MEMS switch with peak isolation of 47.75 dB in 25 GHz to achieve high isolation. Ma et al. (2018) added two short high-impedance transmission lines on both sides of the switch to improve RF performance. Rao et al. (2021a, b) used an asymmetric cantilever structure and perforation to design together to achieve low pull-in voltage.

✉ Chengqi Lai
laichengqi@bupt.edu.cn

Zhongliang Deng
dengzhl@bupt.edu.cn

Jiali Zhou
zhoujiali@bupt.edu.cn

Yucheng Wang
wangyucheng@bupt.edu.cn

[1] School of Electronic Engineering, Beijing University of Posts and Telecommunications, Haidian District, Beijing 100876, China

[2] School of Automation, Beijing University of Posts and Telecommunications, Haidian District, Beijing 100876, China

This paper proposes a novel shunt capacitive RF MEMS switch with low actuation voltage and a high on/off capacitance ratio. As shown in Fig. 1, the switch design adopts a new type of spring structure, in which switch anchor points are in the middle of the serpentine flexure. This structure can obtain a lower elastic coefficient and a low pull-in voltage. Compared with the general method of increasing the capacitance ratio, the method in this paper has the advantage that only one layer of MIM metal is added to achieve a high capacitance ratio of the switch. There is no need to change the air gap g of the switch, avoiding the excessively high g increasing the pull-down voltage of the switch, and not deliberately warping the switch beam, avoiding the uncertainty of the processing technology, and also avoiding the use of new Material.

2 Design of RF MEMS switch and working principle

The shunt capacitive RF MEMS is integrated into the coplanar waveguide (CPW). The G/S/G of CPW is 60 µm/100 µm/60 µm. The anchor of the MEMS switch is connected to the ground of the CPW, which has a thin dielectric layer made of Si_3N_4 to prevent the switch beam from contacting the signal line. An H-shaped floating metal layer is added above the dielectric layer to improve the capacitance ratio of the RF MEMS switch. The actuation electrode is placed below the beam. The holes on the beam are used to reduce squeeze film damping, thereby increasing the switching speed, and the holes can also release part of the residual stress of the beam.

When the DC voltage is applied between the MEMS beam and the microwave transmission line, the generated electrostatic force causes the MEMS beam to collapse down to the dielectric layer, and the switching capacitor will significantly increase. This capacitor connects the transmission line to the ground, forming a short circuit in the microwave frequency, equivalent to a reflective switch, which realizes the off-state of the switch. When no bias voltage is applied, the RF MEMS switch will return to the initial state due to the elastic restoring force of the beam to realize the switch's on-state. Through this paper's design, the switch's pull-in voltage can be obtained through simulation as 4.4 V, and the on/off capacitance ratio of the RF MEMS switch can reach 271.

3 Mechanical analysis

3.1 Electrodes topology and theory analysis

The designed switch can be simplified into a fixed–fixed switch to analyze the relationship between the actuation electrode's size and the switch's elastic coefficient. Figure 2 shows the left-side view of the switch. The electrode positions are set from x to (l-x). In this paper, the driving electrode is located below the switch beam.

The spring constants k of the RF MEMS switch can be divided into the spring constant k_1 caused by the beam stiffness and the spring constant k_2 caused by the biaxial residual stress, which can be obtained by the following equations. (Deng et al. 2022).

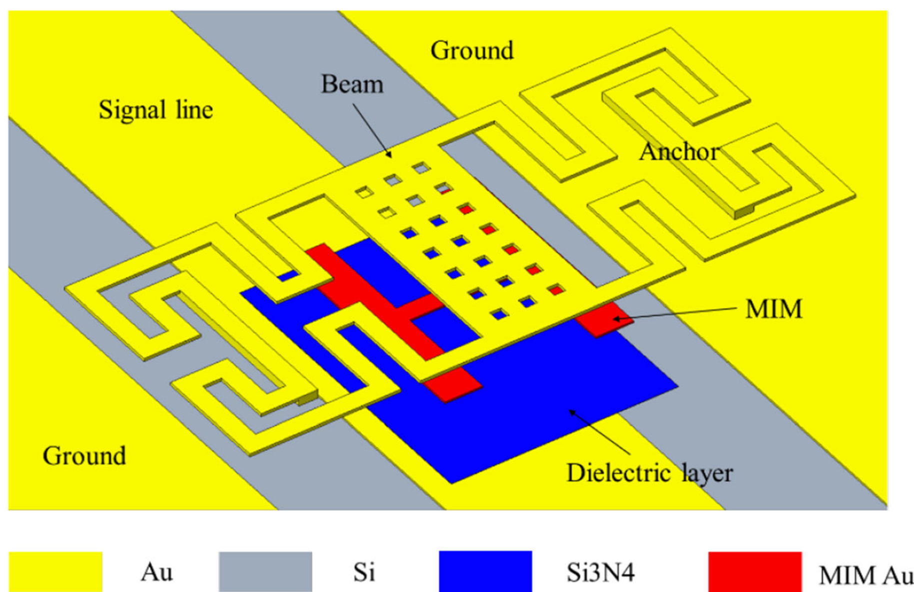

Fig. 1 Proposed switch with MIM capacitor

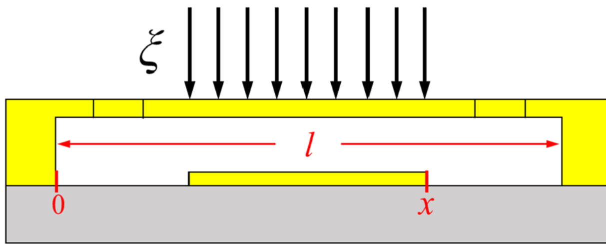

Fig. 2 Electrode topology of the MEMS switch

$$k_1 = -\frac{P}{\frac{2}{EI}\int_{\frac{l}{2}}^{x}\frac{\rho}{48}\left(l^3 - 6l^2a + 9la^2 - 4a^3\right)da} \tag{1}$$

$$k_2 = \frac{P}{2\int_{\frac{l}{2}}^{x}\frac{\rho}{2S}(l-a)da} \tag{2}$$

$$k = k_1 + k_2 \tag{3}$$

$$I = \frac{wt^3}{12} \tag{4}$$

$$P = 2\rho\left(x - \frac{l}{2}\right) \tag{5}$$

$$S = \sigma(1-v)tw \tag{6}$$

l is the length of the beam. ρ is the uniform distributed load of the beam, P is the total load, S is the tensile force of the biaxial residual stress, and σ is the biaxial residual stress.

Figure 3a shows the relationship between elastic coefficient k, beam length l, and x/l. When x/l is determined, the beam length l greatly influences the elastic coefficient k, and k decreases with the increase of l. On the contrary, when the length of the switch beam l is determined, the switch elastic coefficient k increases with the rise of x/l, and the influence of x/l on the switch elastic coefficient k is small. It can also be noticed that the elastic coefficient k_2 due to biaxial residual stress significantly influences the elastic coefficient k. From Fig. 3b, the same rule holds for V_p.

Figure 4 gives the relationship between the pull-in voltage V_p, the biaxial residual stress σ, and the elastic coefficient k. Due to the increase of σ, the elastic coefficient caused by the residual stress increases, leading to the pull-down voltage increase. For a rectangular beam of Au (E = 78 Gpa, v = 0.44), g = 2 µm, x = 140 µm, t = 1.6 μm, σ is less than 30 MPa when V_p is less than 10 V.

3.2 Low spring constant switch design

For the CPW (G/S/G = 60 µm/100 µm/60 µm) in this article, the width of the electrode x has been determined. According to the above analysis, the length l should be lengthened as much as possible to achieve a low elastic coefficient and low driving voltage, but a longer l requires a larger switch area. The structure of the folded-area beam used in this paper places the anchor point in the middle of the meander leg to reduce the switch area. The analysis in 2.1 is only for the design of the general direction, and the above model is not accurate enough for a specific calculation.

The designed spring is shown in Fig. 5 to reduce the spring coefficient of the switch. The energy method is used to solve the elastic coefficient of the designed spring beam. The boundary conditions for the guide-end arm are determined by symmetry, the rotation and displacement of the arm are expressed in the direction of force application, and the force in other directions is assumed to be zero.

The designed spring arm can be divided into nine sections, and the moment M_i and torsion T_i of each section can be obtained through the structural topology of the switch and calculated by Eq. 7.

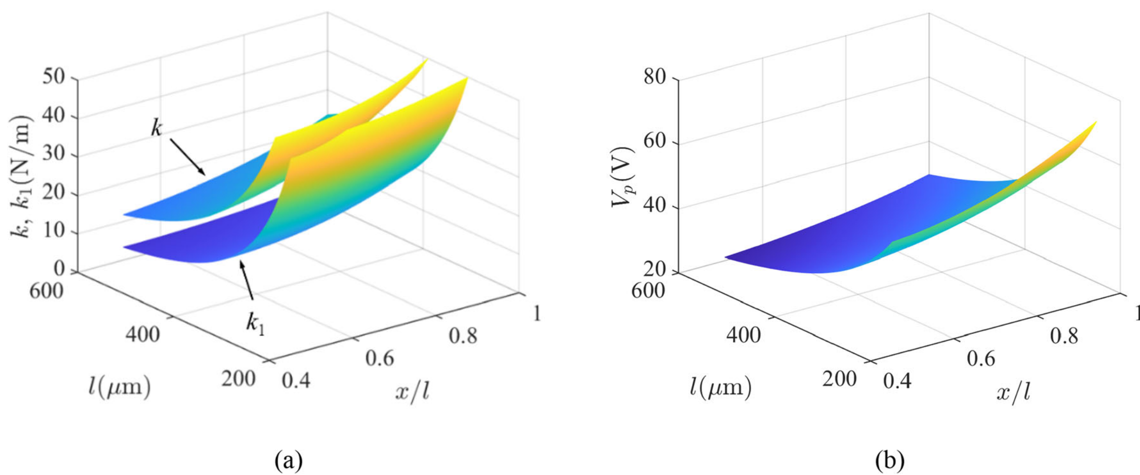

Fig. 3 **a** Relationship between elastic coefficient k, k_1, l, and x/l. **b** Relationship between elastic coefficient V_p, l, and x/l

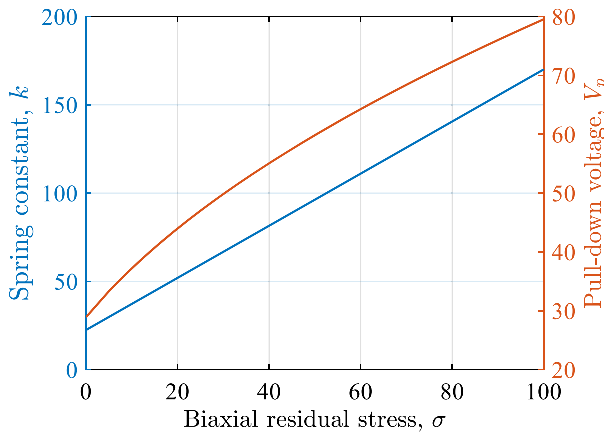

Fig. 4 Relationship between the σ and the k and V_p

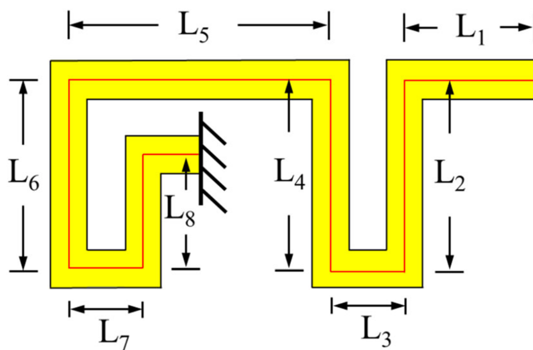

Fig. 5 Equivalent mechanical spring model

$$\begin{aligned}
&M_1 = M_0 - F_z\xi M_6 = T_0 - F_z(L_2 + L_4 + \xi)\\
&T_1 = T_0 T_6 = M_0 - F_z(L_1 + L_3 + L_5)\\
&M_2 = T_0 - F_z\xi M_7 = M_0 - F_z(L_1 + L_3 + L_5 - \xi)\\
&T_2 = M_0 - F_z L_1 T_7 = T_0 - F_z(L_2 + L_4 + L_6)\\
&M_3 = M_0 - F_z(L_1 + \xi)M_8 = T_0 - F_z(L_2 + L_4 + L_6 - \xi)\\
&T_3 = T_0 - F_z L_2 T_8 = M_0 - F_z(L_1 + L_3 + L_5 + L_7)\\
&M_4 = T_0 - F_z(L_2 + \xi)M_9 = M_0 - F_z(L_1 + L_3 + L_5 + L_7 - \xi)\\
&T_4 = M_0 - F_z(L_1 + L_3)T_9 = T_0 - F_z(L_2 + L_4 + L_6 - L_8)\\
&M_5 = M_0 - F_z(L_1 + L_3 + \xi)\\
&T_5 = T_0 - F_z(L_2 + L_4)
\end{aligned} \tag{7}$$

ξ is the direction along the length of each arm, and L_i is the length of each section of the arm.

The boundary conditions are defined in phrases of reaction force, moment, and torsion at the end of each arm by solving the equations as $\sum F = 0$, $\sum M = 0$, $\sum T = 0$ at the end of each arm section. The guided-end constrains bending θ_0 and rotation ϕ_0 at the end of the arm are given by Eq. 8 and Eq. 9 (Saberhosseini et al. 2021):

$$\theta_0 = \frac{\partial U}{\partial M_0} = \sum_{i=1}^{n} \int_0^{L_i} \left(\frac{M_i}{EI_i} \frac{\partial M_i}{\partial M_0} + \frac{T_i}{GJ_i} \frac{\partial T_i}{\partial M_0} \right) d\xi = 0 \tag{8}$$

$$\phi_0 = \frac{\partial U}{\partial T_0} = \sum_{i=1}^{n} \int_0^{L_i} \left(\frac{M_i}{EI_i} \frac{\partial M_i}{\partial T_0} + \frac{T_i}{GJ_i} \frac{\partial T_i}{\partial T_0} \right) d\xi = 0 \tag{9}$$

After finding M_0 and T_0, substituting them back into Eq. (1), and using Castigliano's second theorem, the vertical displacement can be obtained by Eq. (4). (Meriam and Kraige 2011)

$$\delta_z = \frac{\partial U}{\partial F_z} = \sum_{i=1}^{n} \int_0^{L_i} \left(\frac{M_i}{EI_i} \frac{\partial M_i}{\partial F_z} + \frac{T_i}{GJ_i} \frac{\partial T_i}{\partial F_z} \right) d\xi \tag{10}$$

where:

$$G = \frac{E}{2(1 + v)} \tag{11}$$

$$J = \frac{1}{3} - \frac{64}{\pi^5} \frac{t}{w} \sum_{m=1,3,5,7\cdots}^{\infty} \frac{\tanh \frac{m\pi w}{2t}}{m^5} \tag{12}$$

G is the shear modulus, w is the width of the beam, t is the thickness of the beam, v is the Poisson's ratio, I is the moment of inertia, and E is Young's modulus. For a torsion bar with a narrow and long rectangular cross-section, J can be taken as 1/3.

The spring constant in the z-direction for an arm represents by Eq. 13 (Sravani et al. 2021). Since the four arms are in a parallel relationship, the final elastic coefficient is obtained by Eq. 14.

$$k_{arm} = \frac{F_z}{\delta_z} \tag{13}$$

$$k_{eq} = 4k_{arm} \tag{14}$$

3.3 Pull-in voltage and switch time

The parameters of the proposed structure are shown in Table 1. Through the above analysis, it can be obtained by calculation that when t = 1.6 μm, k is 1.80 N/m, when t = 1 μm, k is 0.44 N/m, and when t = 0.6 μm.

Table 1 Physical dimensions of the switch

Symbol	Value
L_1	35 μm
L_2	50 μm
L_3	20 μm
L_4	50 μm
L_5	55 μm
L_6	50 μm
L_7	20 μm
L_8	30 μm
w	10 μm

The 3D view of the membrane's displacement and von Mises stress distribution at the actuated state is displayed in Fig. 6

Figure 7 shows the four resonant frequency modes of the switch proposed using the COMSOL Multiphysics. Through FEM simulation software, it can be calculated that when $t = 1.6$ μm, k is 1.81 N/m, when $t = 1$ μm, k is 0.46 N/m, and when $t = 0.6$ μm, k is 0.13 N/m. The theoretical calculation is consistent with the model simulation.

In Fig. 8, the relationship between the actuation voltage and the displacement of the switch beam is obtained through Eq. 15. (Bansal et al. 2020)

$$V_p = \sqrt{\frac{8kg^3}{27\varepsilon_0 A}} \tag{15}$$

g is the gap between beam and CPW, ε_0 is the dielectric constant in the free space, and A is the beam and electrode overlap area.

The error between simulation and calculation is less than 4.5%. The analysis agrees well with the simulation.

Figure 9 shows the relationship between the actuation voltage and the switching displacement and switching speed when the actuation voltage is set to 10 V and the voltage rise time is set to 10 μs. Figure 8a shows that when $t = 0.6$ μm, the response time is about 14 μm, when $t = 1$ μm, the response time is about 22 μs, and when $t = 1.6$ μm, the response time is about 39 μs. Figure 8b shows the speed response of the switch when a voltage is applied. The relationship between the speed of the beam and the time is linearly increasing at the beginning, and then the speed has a sudden change, and it quickly drops to 0 m/s after reaching the maximum value. The reason is that the capacitance between the switch and the signal line will gradually increase during the pull-in process of the switch, and the electrostatic force will also increase. When a certain distance is reached, the electrostatic force will be much greater than the elastic force of the spring, resulting in a pull-in effect and a rapid speed. When the switch is fully closed, the switching speed is reduced to 0 m/s.

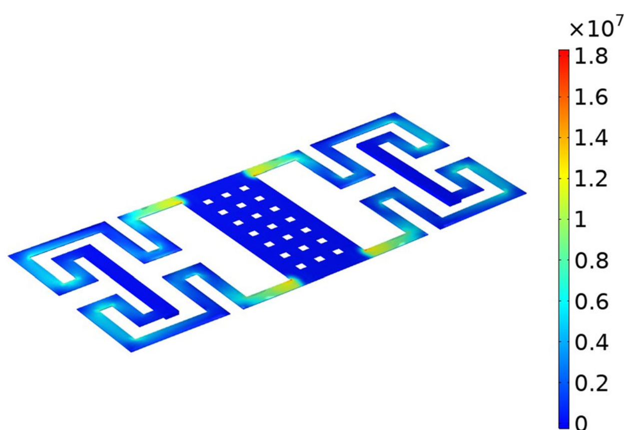

Fig. 6 Von Mises stress distribution

4 Design of high on/off capacitance ratio RF MEMS switch

The on/off capacitance ratio is increased by increasing the down-state capacitance or decreasing the up-state capacitance. However, due to the dielectric layer's pinhole problem, we cannot deposit Si_3N_4 layers thinner than 0.1 μm. The dielectric layer should withstand the excitation voltage without being pierced. Therefore, it is not easy to further increase the down-state capacitance. On the other hand, the on-state capacitance can be reduced by increasing the air gap, but the increase of the air gap will increase the pull-in voltage of the switch.

This paper increases the switch's capacitance ratio by adding an H-shaped floating metal layer. As shown in Fig. 10a, the floating metal layers are covered on both sides of the switch and connected by a thin metal connecting line. When the switch is in the up-state as shown in Fig. 10b, the MAM (metal-air-metal) capacitor generated by the switch beam and the floating metal is in series with MIM (metal–insulator-metal) capacitor generated by the floating metal and the signal line, which reduces the up-state capacitance. When the switch is in the down-state, as shown in Fig. 9c, the switch beam is in contact with the floating metal layer. The area of the down-state capacitor is the sum of the floating metal layer's area and the switch beam's area, which increases the down-state capacitance. Thereby, the high capacitance ratio is obtained.

4.1 Equivalent circuit topology

As shown in Fig. 11, the H-shaped floating metal layer is divided into three parts to calculate the switch capacitance ratio, namely A_0, A_1, and A_2. A_0 and the signal line produce the MIM capacitor C_1, the MIM capacitor C_2 is produced by A_1 and the signal line, A_1 and the switch beam produce the MAM capacitor C_3. The capacitor without the floating metal layer is C_4.

Figure 12 gives the topology of the switch circuit after adding a floating metal layer. Where C_u is the equivalent up-state capacitance of the switch, C_d is the equivalent down-state capacitance of the switch, g is the gap between the beam and the dielectric layer, L is the equivalent inductance of the switch, and R_s is the equivalent resistance of the switch. When the switch is in the down state, the beam is in contact with the MIM, and the designed switch is the same as the general switch, which can be equivalent to a series resonant circuit (Rebeiz GM 2003). C_d can be calculated by publicizing the parallel plate capacitor. When

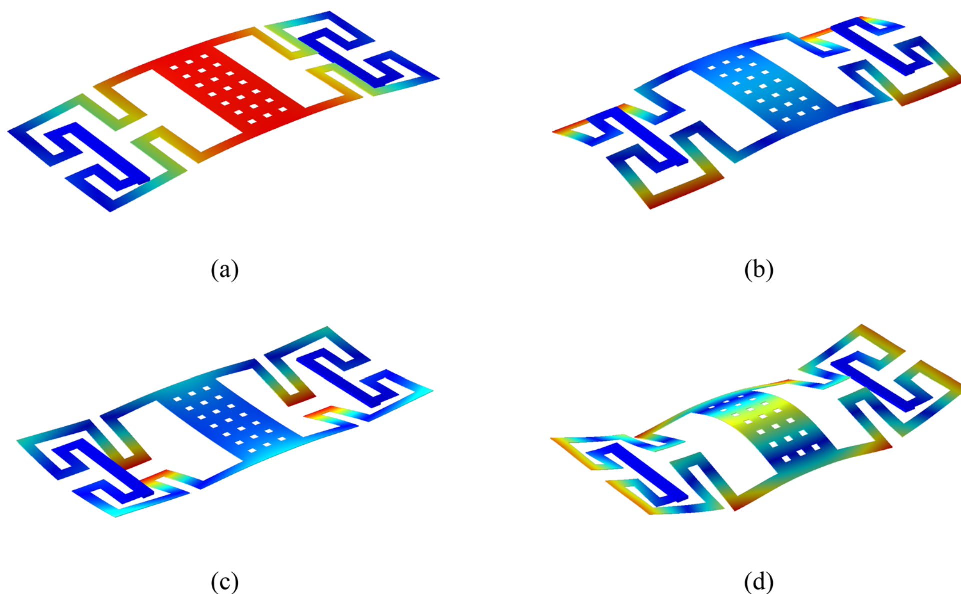

Fig. 7 The first six modes of resonance frequency in the proposed device. **a** 4345.2 Hz **b** 21414 Hz **c** 22994 Hz **d** 42171 Hz

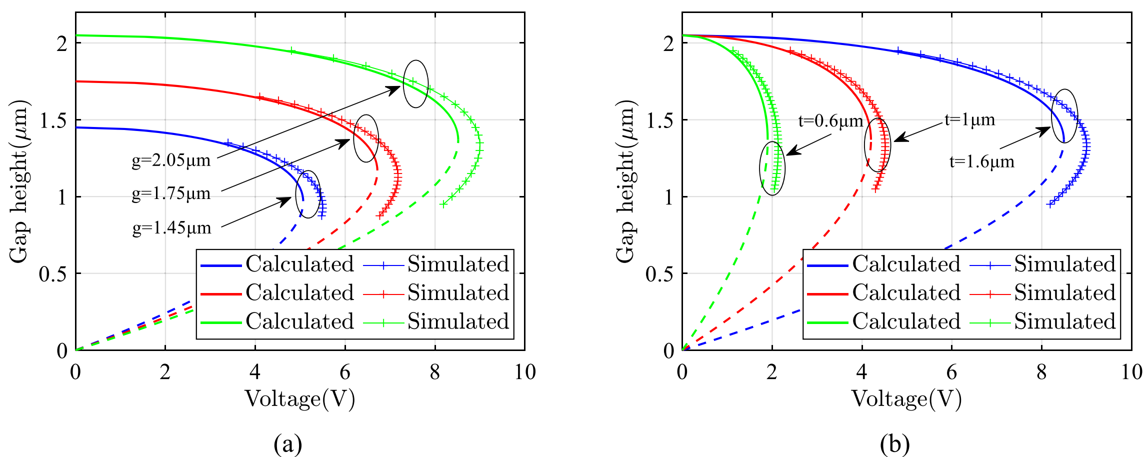

Fig. 8 Relationship between gap height and actuation voltage. **a** Curves under different g values when t = 1.6 μm **b** Curves under different t values when g = 2.05 μm

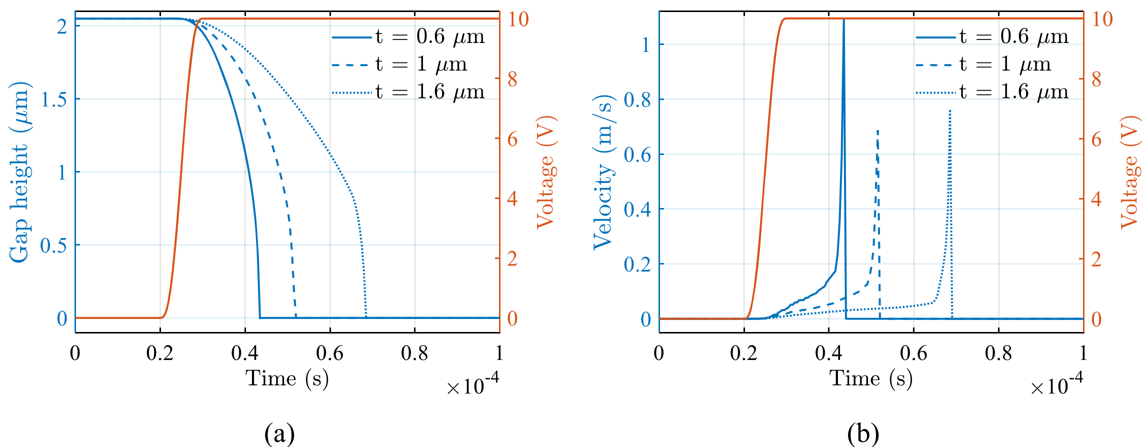

Fig. 9 Transient response of the switch with different thicknesses. **a** Relationship between displacement and time **b** Relationship between the velocity of the switch and time

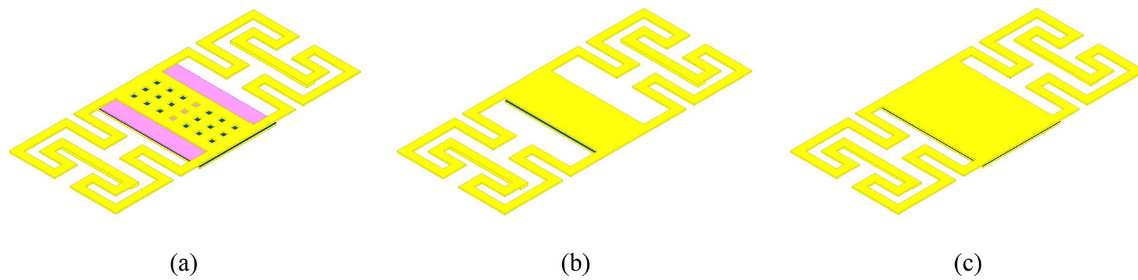

Fig. 10 Models of the proposed switch. a 3D model b Equivalent model of up-state models of the proposed switch. c Equivalent model of down-state models of the proposed switch

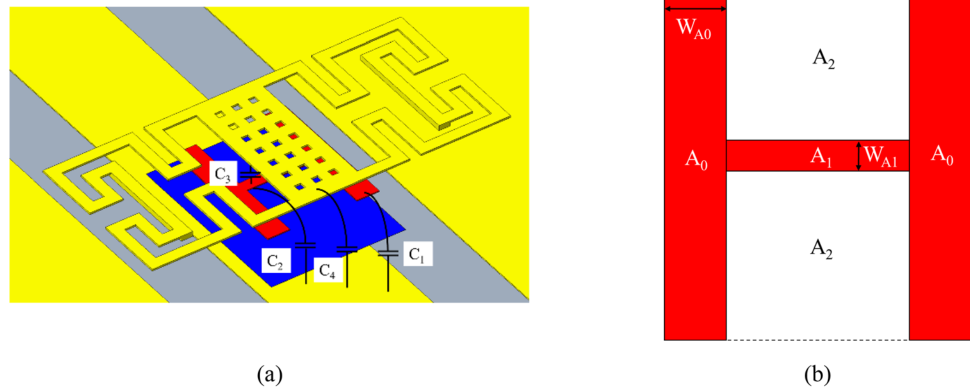

Fig. 11 Floating metal layer diagram

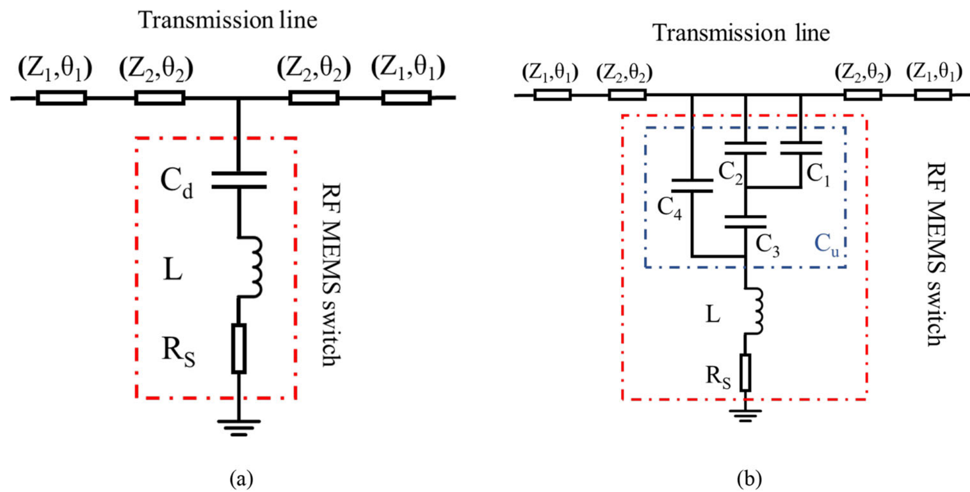

Fig. 12 Circuit topology of MEMS switches with floating metal layer a circuit models of down-state MEMS switches b circuit model of up-state MEMS switch

the switch is in the up-state, C_u is composed of MIM capacitors and MAM capacitors. In Fig. 12, C_u is equivalent to a combination of four capacitors, and the edge effect of capacitors is ignored here.

According to Fig. 12, the up-state capacitance and down-state capacitance of the switch can be obtained by following equations,

$$C_u = (C_1||C_2 + C_3)||C_4 \tag{16}$$

$$C_1 = \frac{\varepsilon_0\varepsilon_r A_0}{t_d} \tag{17}$$

$$C_2 = \frac{\varepsilon_0\varepsilon_r A_1}{t_d} \tag{18}$$

$$C_3 = \frac{\varepsilon_0 A_1}{g} \tag{19}$$

$$C_4 = \frac{\varepsilon_0 A_2}{g + \frac{t_d}{\varepsilon_r}} \tag{20}$$

Fig. 13 Analysis of Cr **a** Relationship among C_r, λ_1 and λ_2 **b** Relationship among Cr, t_1 and g

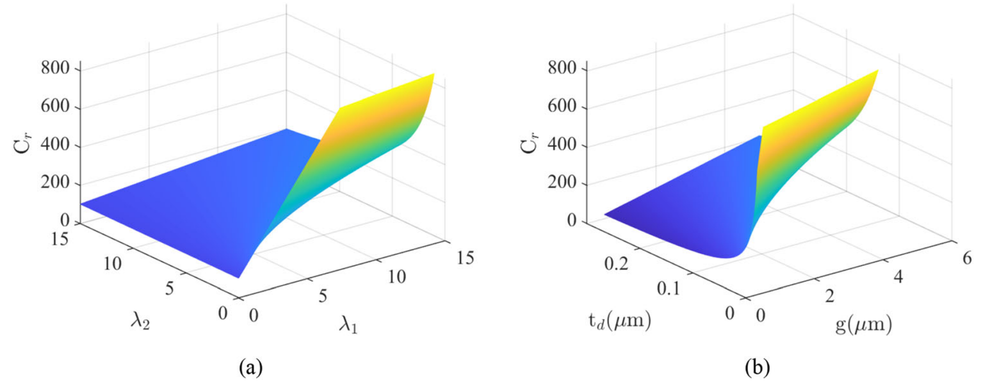

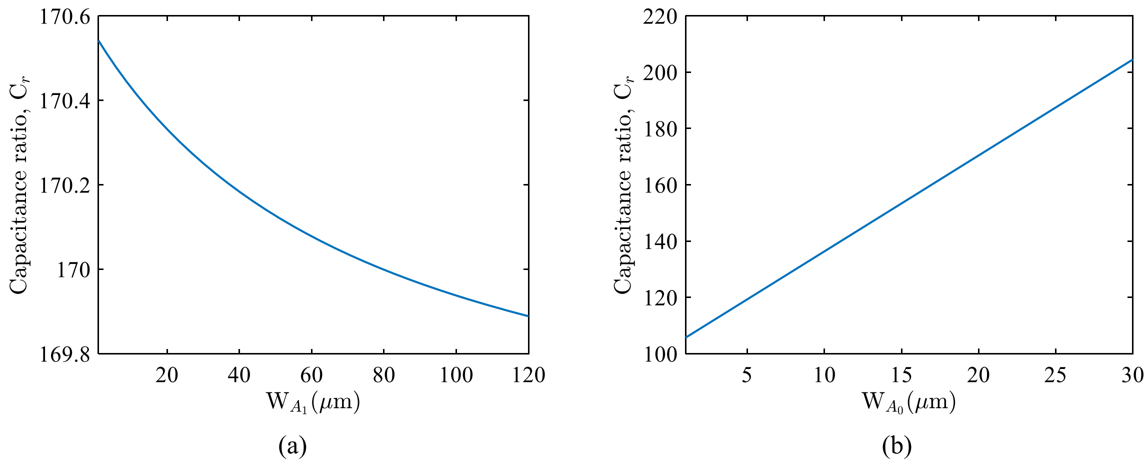

Fig. 14 The relationship among the value of C_r, W_{A1}, and W_{A0}. **a** The relationship between the value of C_r and W_{A1} **b** The relationship between the value of C_r and W_{A0}

$$C_d = \frac{\varepsilon_0 \varepsilon_r (A_0 + A_1 + A_2)}{t_d} \tag{21}$$

The capacitance ratio C_r is obtained by Eq. 22.

$$C_r = \frac{(A_0 + A_1 + A_2)(\varepsilon_r g + t_d)(A_1 t_d + \varepsilon_r g(A_0 + A_1))}{t_d(A_1(A_0 + A_1)(\varepsilon_r g + t_d) + A_2(A_1 t_d + \varepsilon_r g(A_0 + A_1)))} \tag{22}$$

To explore the relationship between the size of the floating metal layer and the capacitance ratio, let $A_0 = \lambda_1 A_1$, $A_2 = \lambda_2 A_1$ get:

$$C_r = \frac{(1 + \lambda_1 + \lambda_2)(\varepsilon_r g + t_d)(t_d + \varepsilon_r g(1 + \lambda_1))}{t_d((1 + \lambda_1)(\varepsilon_r g + t_d) + \lambda_2(t_d + \varepsilon_r g(1 + \lambda_1)))} \tag{23}$$

4.2 Switch on/off capacitance ratio analysis

Figure 13a gives the relationship between C_r and λ_1, λ_2. When λ_1 is determined, the capacitance ratio C_r increases with the increase of λ_2, but the change is small. When λ_2 is determined, the capacitance ratio C_r will increase rapidly with the rise of λ_1. A_1 contributes less to reducing the up-state capacitance, while A_0 contributes more to improving the capacitance ratio. The capacitor generated by the switch's beam and the signal line does not change significantly due to the change of λ_2.

The relationship between the switch capacitance ratio C_r, t_d, and g is shown in Fig. 10b. C_r will increase with the decrease of t_d. When t_d is less than 0.1 μm, C_r increase will increase sharply. However, the t_d will be designed to be above 0.1 μm to ensure that the dielectric layer will not be pierced by actuation voltage. On the other hand, C_r also increases with the increase of g. Because the range of g is large, the influence of g on the capacitance ratio is more significant than that of t_d.

To further discuss the effect of the shape of the floating metal layer on the capacitance ratio, W_{A1} and W_{A0} are analyzed in Fig. 14. When W_{A1} increases, C_2 and C_3 become larger, and the up-state capacitance increases, resulting in a decrease in the capacitance ratio. However, the up-state capacitance is connected in parallel with C_4, so it has little effect on the capacitance ratio. When W_{A0} increases, the switch capacitance ratio increases significantly due to the increase of the switch down-state

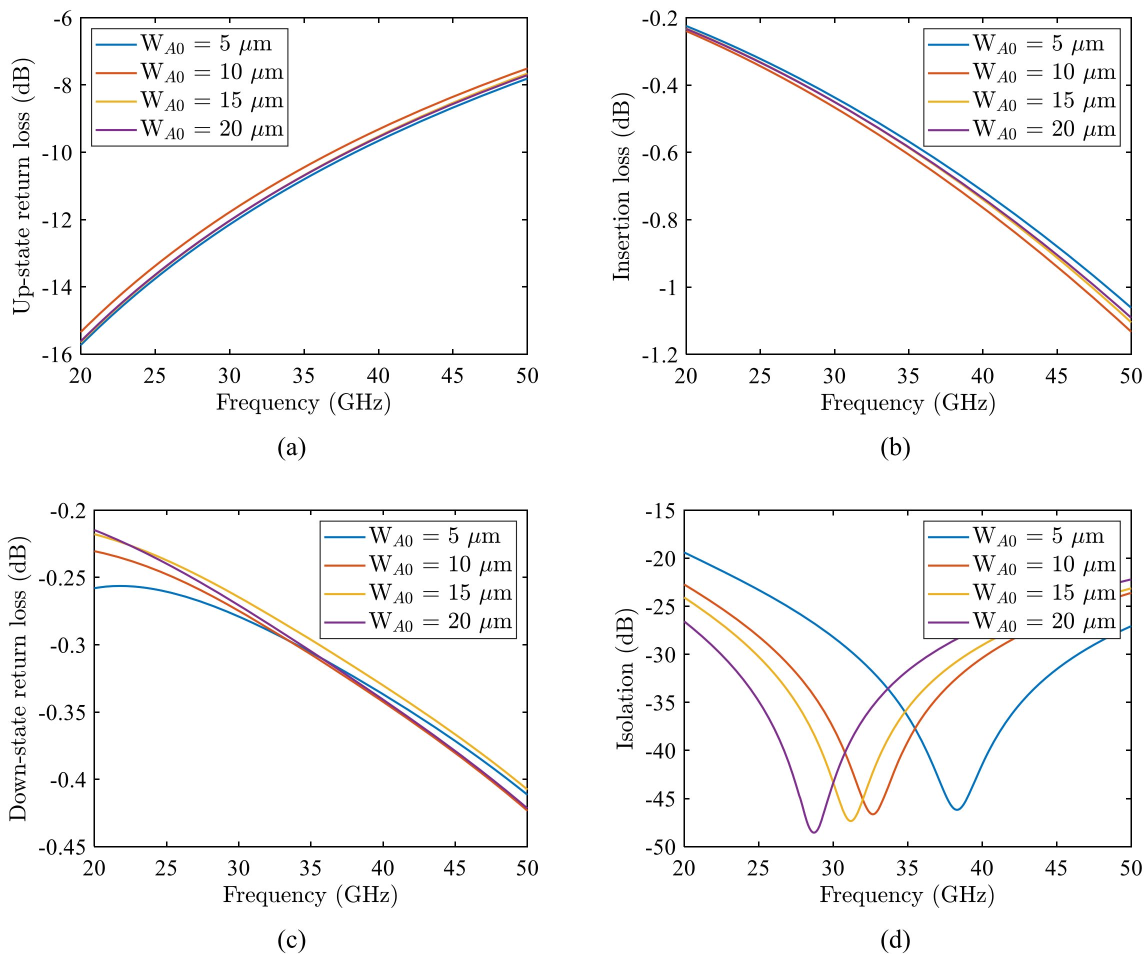

Fig. 15 S_{12} and S_{11} of the proposed switch. **a** Up-state return loss **b** Insertion loss **c** Down-state return loss **d** Insolation

capacitance, which improves the switch on/off capacitance ratio. In this paper, W_{A0} = 20 μm, W_{A1} = 10 μm.

5 RF performance of the proposed switch

5.1 S-parameters

Finally, the S-parameters of the proposed switch is analyzed according to the size of the floating metal layer. As shown in Fig. 15, W_{A0} has no great influence on the return loss of the upper and lower states of the switch and the isolation. The return loss of the switch at 36 GHz is about − 10 dB, the insertion loss is about − 0.6 dB, and the return loss of the lower state is about − 10 dB. The loss is about − 0.3 GHz. W_{A1} greatly influences the center frequency of isolation when W_{A1} changes from 5 µm to 20 µm. The switching frequency drops from 38 to 29 GHz with a peak of about − 48 dB. This is mainly because the increase of the MIM area will obviously affect the switch's upper and lower state capacitances, which will cause the center frequency of the switch to shift.

The above rules are also applicable to W_{A1}. As shown in Fig. 16, W_{A1} has no great influence on the return loss of the up and down states of the switch and the isolation. When the switch is at about 35 GHz, the return loss of the upper state is about − 10 dB, and the insertion loss at 35 GHz is about − 0.6 dB, and the return loss in the lower state is about − 0.3 GHz. When W_{A1} varies from 10 µm to 100 µm. Switching frequency down from 29 to 18 GHz with a peak of about − 50 dB.

5.2 Capacitance ratio of the proposed RF MEMS switch

The switch capacitance ratio can be obtained through the above results. Up-state return loss (S_{11}) and isolation (S_{21}) are important parameters to characterize the RF performance of RF-MEMS switches and use them to calculate C_u and C_d by Eqs. 24 and 25, respectively. (Rebeiz GM 2003)

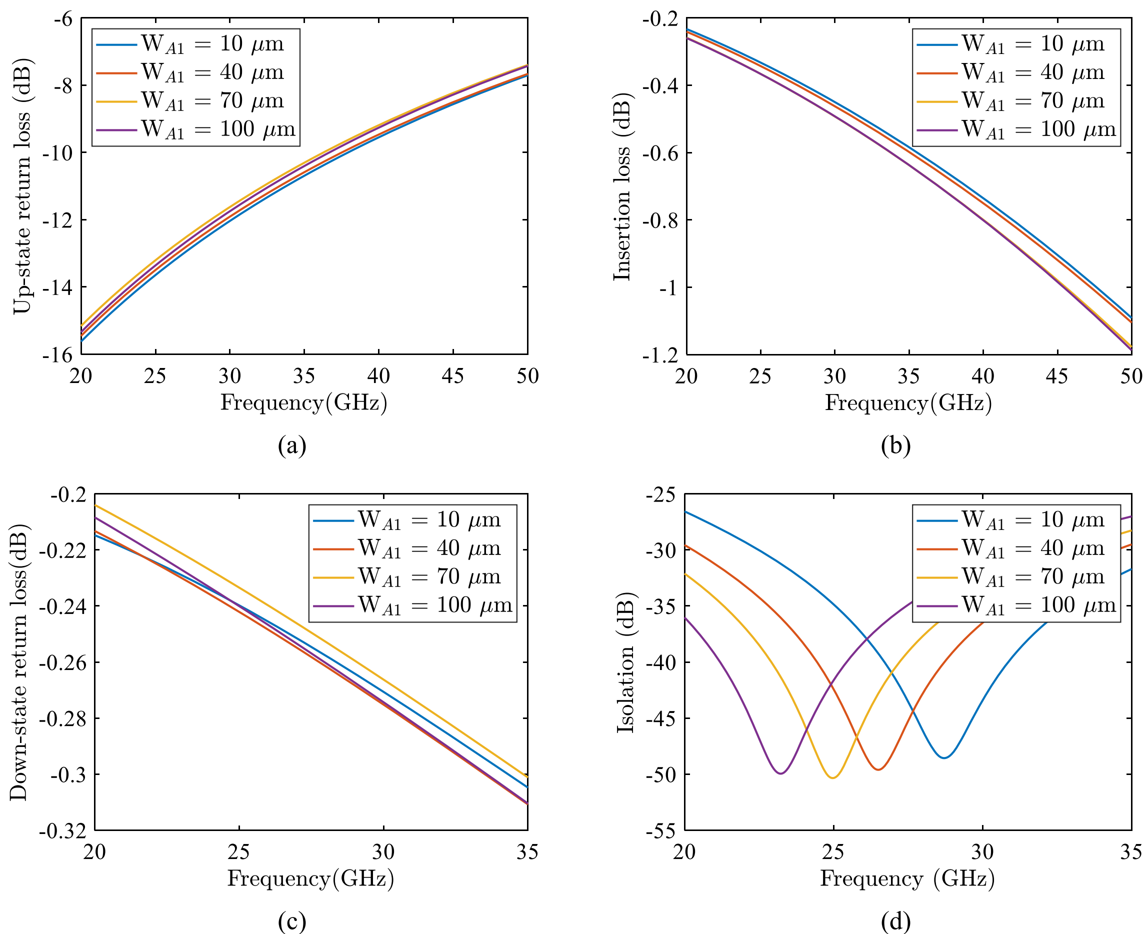

Fig. 16 S_{12} and S_{11} of the proposed switch. **a** Up-state return loss **b** Insertion loss **c** Down-state return loss **d** Insolation

$$|S_{11}|^2 \approx \frac{\omega^2 C_u^2 Z_0^2}{4} \tag{24}$$

$$|S_{21}|^2 \approx \frac{4}{\omega^2 C_d^2 Z_0^2} \tag{25}$$

For the switch proposed in this paper, C_u = 217.4 fF and C_d = 58.99 pF. A capacitance ratio of 271 can be obtained. When the MIM capacitor is not used, the on/off capacitance ratio obtained by the above method is 102. The switch capacitance ratio is greatly improved in the presence of the MIM capacitor.

6 Measurement and discussion

The switches are machined at the foundry and then tested. Figure 17 shows a photograph of the proposed RF MEMS switch.

Figure 18 shows the connection diagram of the test platform. The bias voltage of the switch is provided by E3631A, and S11 and S12 of the switch are measured by a vector network analyzer (R&S ZVA50, Rohde & Schwarz, Munich, Germany). Measurement probes were ACP-A-GSG-150 probes (Cascade Microtech, Beaverton, OR, USA). The probe station equipment is (Cascade Summit

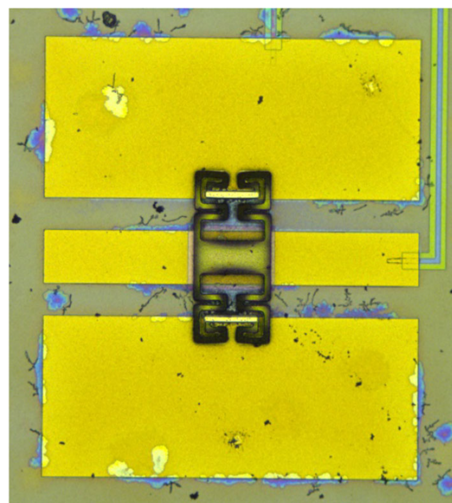

Fig. 17 Photograph of the proposed RF MEMS switch

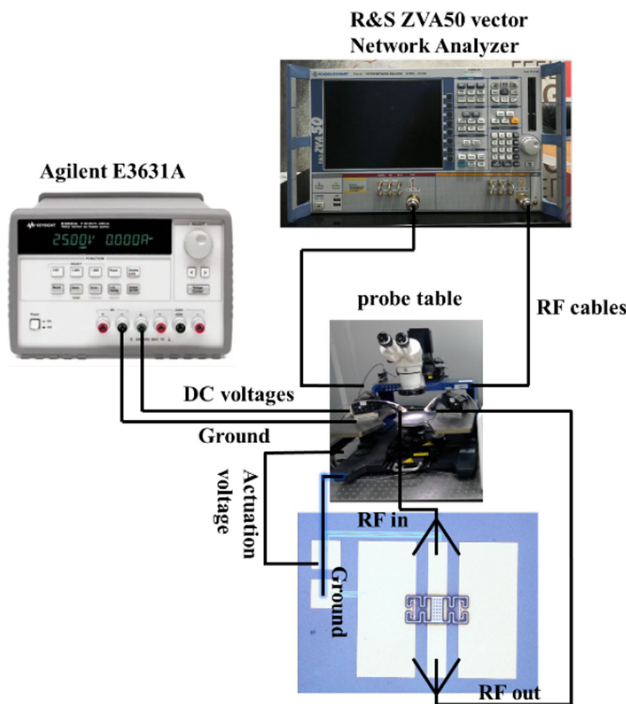

Fig. 18 Schematic diagram of switch test

11000B-M, Cascade Microtech, Beaverton, OR, USA), and the scanning frequency is 10 MHz $\sim$ 40 GHz.

Figure 19 shows the simulation and test comparison of the switch, where the solid line is the test data, and the dotted line is the simulation data.

The measurements of the up-state S11, the down-state S11, and the insertion loss agree with the simulation. The insertion loss at 20 GHz–30 GHz is − 0.3 dB, the return loss in the up-state is − 20 dB and the down-state's return loss is − 0.5 dB. In terms of isolation, there is a certain gap between the simulation value and the measured value The measured value is − 24 dB, and the simulated value can reach − 48 dB. This is mainly caused by the reduction of the air gap g caused by the processing of the middle MIM metal layer and the release of the sacrificial layer. On the other hand, it can be noticed that although the isolation of the switch has decreased, the simulation and measurement agree well at the switching frequency point. This is because the MIM metal avoids the frequency deviation caused by the warping of the switch. When the switch beam touches MIM, the down-state capacitance is no longer affected by switch warping due to the existence of MIM, so no frequency offset will occur. Through calculation, the actual capacitance ratio is 89.

The RF MEMS designed in this paper only needs to add a layer of MIM metal to achieve an increase in capacitance ratio without changing the air gap g of the switch, using new materials, and relying on uncertain warpage. At the same time, according to the above analysis, it can be obtained that controlling the area of the MIM can achieve a wide range of frequency changes when using switches with the same area, and the design process can be simplified for different frequency requirements. The designed switch can be used in reconfigurable fields, such as phased array antennas, reconfigurable smart metasurfaces, and tunable bandpass filters, etc. The problem is that it is difficult to solve the problem of warping the thinner spring legs in the process.

7 Conclusion

In this paper, a novel RF MEMS switch is designed. The switch consists of novel serpentine beams as switch legs, which reduces the pull-in voltage. When the thickness of the switching beam is 1 μm, the pull-in voltage is 4.4 V, and the switching time is calculated as 22 μs. By adding an H-shaped MIM capacitor, the on/off capacitance ratio of

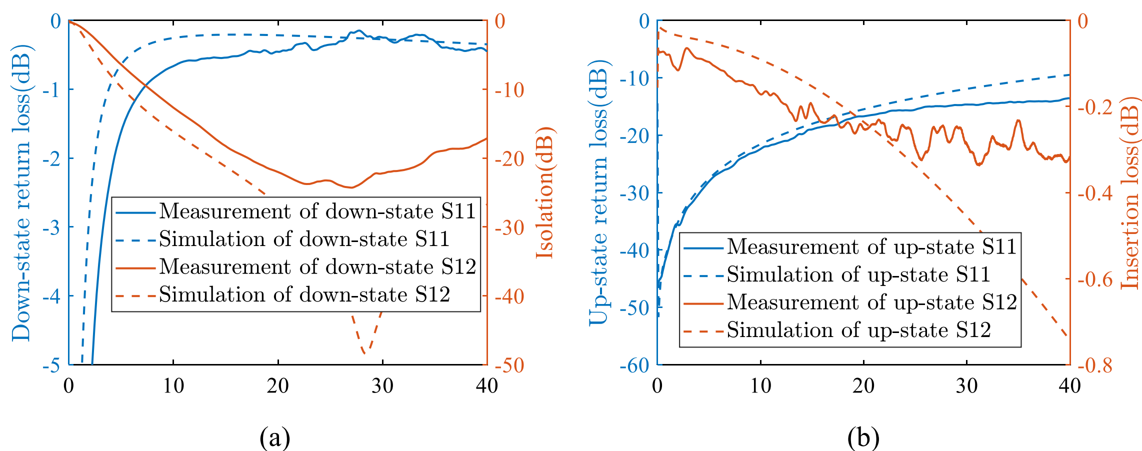

Fig. 19 Simulation and test comparison of the switch

Table 2 Comparison of the proposed device parameters with previous works

Author	Insertion loss	Isolation	C_r	Actuation voltage	Actuation time
Badia et al. (2012)	− 0.68 dB@24 GHz	− 35 dB@40 GHz	9.87	21.8 V	–
Mafinejad et al. (2017)	− 0.9 dB@24 GHz	− 18 dB @24 GHz	12–20	20 V	3 µs
Ma et al. (2018)	− 0.25 dB@20 GHz	− 27.4 dB @20 GHz	60	2.2 V	27 µs
Maninder et al. (2019)	− 0.025@8Gz	20 dB @ 7 GHz	77.4	12.25	–
Ansari et al. (2020)	− 0.3 dB@33 GHz	− 57 dB@33 dB	64	9.2 V	36.2 µs
Deng et al. (2022)	− 0.2 dB@30 GHz	− 41 dB@22 GHz	162	4.5 V	71 µs
Dalal et al. (2021)	0.6 dB@32 GHz	− 47@32 GHz	–	3 V	–
Rao et al (2021a, b)	0.25@22 GHz	− 37@22 GHz	10	8 V	1.2 ms
Kumari et al.(2022)	0.5@40 GHz	− 34@16 GHz	–	15.4	–
Sharaf (2022)	–	–	66.7	24.1	45 µs
This work	− 0.25 dB@27 GHz	− 47.4 dB @27 GHz	89	4.4 V	22 µs

the switch is greatly improved without affecting the switch structure and materials, and the on/off capacitance ratio is 89. Table2 presents the comparison between the proposed switch and previous switches in recent years. Due to its excellent performance, the proposed switch is ideal for reconfigurable and communication systems.

Data availability All relevant data are within the paper.

References

Al-Dahleh R, Mansour RR (2010) High-capacitance-ratio warped-beam capacitive MEMS switch designs. J Microelectromech Syst 19(3):538–547. https://doi.org/10.1109/JMEMS.2010.2048012

Angira M, Rangra K (2015) Performance improvement of RF-MEMS capacitive switch via asymmetric structure design. Microsyst Technol 21(7):1447–1452. https://doi.org/10.1007/s00542-014-2222-8

Angira M, Sundram GM et al (2013) On the investigation of an interdigitated, high capacitance ratio shunt RF-MEMS switch for X- band applications. Tech Proceed 2013 NSTI Nanotechnol Conf Expo NSTI Nanotech 2:189

Ansari HR, Kordrostami Z (2020) Development of a low stress RF MEMS double-cantilever shunt capacitive switch. Microsyst Technol 26:2739–2748. https://doi.org/10.1007/s00542-020-04838-1

Bansal D, Bajpai A, Kumar P, Kaur M, Kumar A (2020) Effect of stress on pull-in voltage of RF MEMS SPDT switch. IEEE Trans Elect Dev 67(5):2147–2152. https://doi.org/10.1109/TED.2020.2982667

Dalal K, Singh T, Singh PK (2021) Optimized vertical RF-MEMS switch design with a small actuation voltage. Analog Integr Circ Sig Process 108:165–171. https://doi.org/10.1007/s10470-021-01846-7

Deng K, Yang F, Deng Z et al (2021) Analysis and design of a novel high capacitance ratio and low actuation voltage RF MEMS switch. Microsyst Technol 27(7):2803–2813. https://doi.org/10.1007/s00542-020-05070-7

Deng Z, Wang Y et al (2022) Novel high isolation and high capacitance ratio RF MEMS switch: design analysis and performance verification. Micromachines 13:646. https://doi.org/10.3390/mi13050646

Fernandez-Bolanos Badia M, Buitrago E, Ionescu AM (2012) RF MEMS shunt capacitive switches using AlN compared to Si_3N_4 dielectric. J Microelectromech Syst 21(5):1229–1240. https://doi.org/10.1109/JMEMS.2012.2203101

Fouladi S, Mansour RR (2010) Capacitive RF MEMS switches fabricated in standard 0.35 µm CMOS technology. IEEE Trans Microwave Theory Tech 58(2):478–486. https://doi.org/10.1109/TMTT.2009.2038446

Gopalan A (2018) Kommuri UK (2018) Design and development of miniaturized low voltage triangular RF MEMS switch for phased array application. Appl Surf Sci 449:340–345. https://doi.org/10.1016/j.apsusc.2018.02.210

Kumari R, Angira M (2022) (2022) FEM simulation and material selection for enhancing the performance of a RF-MEMS capacitive switch. J Comput Electron 21:814–825. https://doi.org/10.1007/s10825-022-01905-w

Ma LY, Nordin AN, Soin N (2018) A novel design of a low-voltage low-loss T-match RF MEMS capacitive switch. Microsyst Technol 24:561–574. https://doi.org/10.1007/s00542-017-3577-4

Mafinejad Y, Kouzani A, Mafinezhad K et al (2017) Low insertion loss and high isolation capacitive RF MEMS switch with low pull-in voltage. Int J Adv Manuf Technol 93:661–670. https://doi.org/10.1007/s00170-017-0558-9

Maninder K, Bansal D, Soni S et al (2019) (2019)On characterization of symmetric type capacitive RF MEMS switches. Microsyst Technol 25:729–734. https://doi.org/10.1007/s00542-018-4006-z

Meriam JL, Kraige LG (2011) Engineering mechanics: statics. Wiley, USA

Mousavi M, Alzgool M, Towfighian S (2021) Electrostatic levitation: an elegant method to control MEMS switching operation. Nonlinear Dyn 104:3139–3155. https://doi.org/10.1007/s11071-021-06499-9

Persano A, Quaranta F, Cola A et al (2010) Ta_2O_5 thin films for capacitive RF MEMS switches. J Sens. https://doi.org/10.1155/2010/487061

Rao KS, Sailaja BVS, Vineetha KV et al (2021a) Design and analysis of asymmetric structure capacitive RF MEMS shunt switch.

Microsyst Technol 27:503–513. https://doi.org/10.1007/s00542-018-4039-3

Rao KS, Kumar PA, Guha K et al (2021b) (2021) Design and simulation of fixed–fixed flexure type RF MEMS switch for reconfigurable antenna. Microsyst Technol 27:455–462. https://doi.org/10.1007/s00542-018-3983-2

Rebeiz GM (2003) RF MEMS: theory, design, and technology. Wiley

Saberhosseini SS, Azizollah Ganji B et al (2021) The mechanical modeling of a special variable MEMS capacitor. Microsyst Technol 27(3):813–820. https://doi.org/10.1007/s00542-020-04969-5

Sharaf A, Nasr A, Elshurafa AM et al (2022) Design analysis and simulation of a digital RF MEMS varactor with high capacitive ratio. Microsyst Technol 28:1831–1844. https://doi.org/10.1007/s00542-022-05318-4

Sravani KG, Narayana TL, Guha K et al (2021) Role of dielectric layer and beam membrane in improving the performance of capacitive RF MEMS switches for Ka-band applications. Microsyst Technol 27:493–502. https://doi.org/10.1007/s00542-018-4038-4

Xu Y, Tian Y, Zhang B et al (2018) A novel RF MEMS switch on frequency reconfigurable antenna application. Microsyst Technol 24:3833–3841. https://doi.org/10.1007/s00542-018-3863-9

Zareie H, Rebeiz GM (2013) High-power RF MEMS switched capacitors using a thick metal process. IEEE Trans Microw Theory Tech 61(1):455–463. https://doi.org/10.1109/TMTT.2012.2226744

Publisher's Note Springer Nature remains neutral with regard to jurisdictional claims in published maps and institutional affiliations.

Springer Nature or its licensor (e.g. a society or other partner) holds exclusive rights to this article under a publishing agreement with the author(s) or other rightsholder(s); author self-archiving of the accepted manuscript version of this article is solely governed by the terms of such publishing agreement and applicable law.